


Dissipative soliton combs with spectral filtering

M. Bataille-Gonzalez and M. G. Clerc 

Departamento de Física and Millennium Institute for Research in Optics, Facultad de Ciencias Físicas y Matemáticas, Universidad de Chile, Casilla 487-3, Santiago, Chile

B. Kostet, Y. Soupart , and M. Tlidi 

Faculté des Sciences, Département de Physique, Université libre de Bruxelles (U.L.B.), C.P. 231, Campus Plaine, B-1050 Bruxelles, Belgium



(Received 20 October 2024; accepted 18 July 2025; published 5 August 2025)

The paradigmatic Lugiato-Lefever model describes the electric field envelope in a ring cavity filled with a Kerr medium and driven by a coherent injected laser beam. This model is applied to the formation of frequency combs associated with localized structures in micro and macroresonators. Including temporal filtering, we derive a generalized Lugiato-Lefever equation. This equation includes diffusion, linear, and nonlinear convection, and third-order dispersion with *purely imaginary* coefficients. Multiscale analysis enables us to disregard higher-order terms, such as nonlinear convection and third-order dispersion. We investigate the formation of periodic and localized structures resulting from the combined action of temporal spectral filtering effect together with Kerr nonlinearity, pumping, dissipation, and frequency detuning. We show that spectral filtering reduces the intensity of the output field and increases the period of traveling solutions. Similarly, the maximum intensity of moving localized structures, often called dissipative solitons, is reduced. In addition, we show that the threshold associated with breathers is shifted toward large input intensities and that the associated domain of existence is significantly reduced. We show that, when the drift is absent, dissipative solitons exhibit a homoclinic snaking bifurcation. Increasing the strength of the temporal filter reduces the pinning range. The presence of the drift breaks the homoclinic snaking and transforms it into isolas of solutions.

DOI: [10.1103/mlqm-6g6h](https://doi.org/10.1103/mlqm-6g6h)

I. INTRODUCTION

Frequency combs generated by continuous-wave (CW) laser output in microcavity Kerr resonators have revolutionized many fields of science and technology [1–4]. Hänsch is credited with being the first to introduce and develop optical frequency combs. These are equally spaced coherent spectral lines [5]. Much attention has been paid to the formation of frequency combs associated with forming Kerr dissipative solitons (DS) of light that maintain their shape during propagation in optical microcavities [6,7]. This simple optical device has a compact size, a high-quality factor, and allows for chip-scale production of frequency combs [8–11]. Kerr-Raman optical frequency combs were also experimentally observed [12–17].

From a fundamental point of view, the Lugiato-Lefever equation (LLE) [18] has led to the prediction and analysis of various phenomena, including the theoretical study of Kerr optical frequency comb generation using whispering gallery mode cavities or integrated ring resonators [19]. In particular, frequency combs as the spectral content of localized light structures were theoretically predicted in driven Kerr resonators before their experimental observation [20,21]. The link between these two objects in micro and macroresonators has been established in [22,23] (see the review [24] in the theme issue [25]). Dissipative solitons are not necessarily stationary. They can exhibit motion or oscillation. In particular, several mechanisms leading to their movement have been de-

scribed in the literature. It has been shown that uniform soliton motion can be induced by Raman scattering [26–28], odd orders of dispersion [29], delayed feedback [30], or spectral filtering [31–36].

The aim is to study the generation of dissipative soliton Kerr combs under the influence of spectral filtering. We consider an optical cavity filled with a Kerr medium, driven by a coherent injected field, and with the inclusion of a temporal spectral filter (see Fig. 1). We reduce the infinite-dimensional discrete Ikeda map to the Lugiato-Lefever equation with spectral filtering. We further simplified the generalized mean-field model by using a global perturbation scheme based on multiple-scale analysis. This approach enables high-order terms, such as the third derivative and nonlinear convection terms, to be suppressed. This approximation is only valid for the law of intensity of the intracavity field and for smooth function transfer. Under these conditions, we show that spectral filtering not only affects the coefficient of the second derivative, but also produces a first derivative whose coefficient is purely imaginary ($i\alpha_1 \partial_\tau E$). In the second part, we study moving dissipative solitons whose spectral contents are frequency combs.

This paper is organized as follows. After briefly presenting a driven Kerr ring resonator with spectral filtering, we derive the mean-field model, the generalized LLE (Sec. II). We present the linear stability analysis of the CW solutions for both anomalous and normal dispersion regimes (Sec. III). Regular moving dissipative structures are then evidenced in the

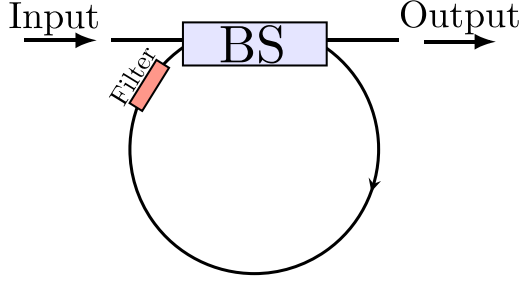


FIG. 1. Schematic setup of a driven ring resonator filled with Kerr media with the filter and driven by a coherent injected field. BS stands for beam splitter. The arrows account for the direction of light propagation.

subcritical modulational instability regime, along with their bifurcation diagrams for the monostable and bistable regimes (Sec. IV. A). The results of the continuation algorithm, which captures the homoclinic snaking bifurcation and isolas associated with dissipative solitons, are presented in Sec. IV. B. We conclude in Sec. V.

II. DERIVATION OF THE MODEL

A. Integrodifferential Lugiato-Lefever model

We consider an optical cavity filled with a Kerr dispersive medium and driven by a coherent plane-wave field as depicted in Fig. 1. Considering the Kerr effect and chromatic dispersion, light propagation in the cavity is governed by the nonlinear Schrödinger equation (NLSE)

$$\frac{\partial F}{\partial z} = i\beta_2 \frac{\partial^2 F}{\partial \zeta^2} + i\gamma |F|^2 F, \quad (1)$$

where F is the slowly varying electric field envelope, z is the longitudinal coordinate along the propagation axis, and ζ is the time in a reference frame traveling at the group velocity of light in the Kerr material. The chromatic dispersion is described by the second derivative with respect to ζ with the coefficient β_2 . The nonlinear coefficient $\gamma = 2\pi n_2/\lambda_0$ with n_2 the nonlinear refractive index and λ_0 is the light wavelength in the vacuum.

In addition to the effects of dispersion and nonlinearity, the field propagating inside the cavity undergoes coherent superposition with the input light beam at the cavity's input beam splitter. This process is described by the following cavity boundary conditions:

$$F^{p+1}(0, \zeta) = \theta F_i + \rho \exp(i\phi) h(\zeta) \otimes F^p(l, \zeta), \quad (2)$$

where parameters ρ and θ are the amplitudes associated with the reflection and the transmission coefficients of the cavity beamsplitter, respectively. For the sake of simplicity, we consider a ring cavity with a single beamsplitter ($\rho^2 + \theta^2 = 1$). Equation (2) provides a relation between the intracavity field envelope F^{p+1} at the input of the cavity after the $p+1$ th round-trip and the field $F^p(l, \zeta)$ at the output after the p th pass in the cavity, where l is the cavity length. The phase $\phi = 2\pi nl/\lambda_0$ represents the linear phase accumulated by the field during a round-trip time t_r , with n as the refractive index. In Eq. (2), the symbol \otimes denotes the causal convolution of the

impulse response function $h(\zeta)$ and the intracavity field F^p after p round-trips. The term $h(\zeta) \otimes F^p(t, \zeta)$ accounts for the temporal filter, where the impulse response function $h(\zeta)$ is a real function.

The nonlinear Schrödinger Eq. (1) supplemented by the cavity boundary conditions, Eq. (2), constitutes an infinite-dimensional map. The set of equations (1) and (2) describes the dynamics of light in the Kerr-type nonlinear ring cavity with a temporal filter. To simplify the theoretical analysis of the problem, it is convenient to reduce this map to a single integrodifferential equation. To do this, we will restrict our analysis to high finesse cavities, i.e., the transmission coefficient θ is supposed to be much smaller than unity. Under this approximation, the temporal evolution of the field inside the cavity is slow for the round-trip time t_r . We can thus consider that this evolution is continuous, and we can replace the map index p with a slow timescale t for the description of the field evolution at the point $z = 0$. The replacement of the round-trip number p by the continuous variable t consists in defining $F(t, \zeta)$ as the cavity pulse envelope at $z = 0$ as

$$F(t = pt_r, \zeta) = F(t, \zeta) = F^p(z = 0, \zeta), \quad (3)$$

where p is a positive integer number. The time t describes the slow evolution of the intracavity field from one round trip to another, while the structure of the intracavity field changes at the fast timescale ζ . The slow-time derivative can be defined as

$$t_r \frac{\partial F(t = pt_r, \zeta)}{\partial t} = F^{p+1}(z = 0, \zeta) - F^p(z = 0, \zeta). \quad (4)$$

The injected field is coupled to the cavity only if the system is close to resonance.

By averaging the right-hand side of the NLSE Eq. (1) over one cavity length, we get

$$F^p(l, \zeta) = F^p(0, \zeta) + i \frac{\beta_2 l}{2} \frac{\partial^2 F^p(0, \zeta)}{\partial \zeta^2} + i\gamma l |F^p(0, \zeta)|^2 F^p(0, \zeta). \quad (5)$$

By taking into account both continuous-time Eq. (3), i.e., $F^p(0, \zeta) = F(t, \zeta)$ and its derivative Eq. (4), i.e., $\partial_t F(t = pt_r, \zeta) = \partial_t F(t, \zeta)$, and by replacing the field amplitude $F^p(l, \zeta)$ that appear in Eq. (5) in the boundary conditions Eq. (4), we obtain

$$t_r \frac{\partial F}{\partial t} = \theta F_i - F + \rho \exp(i\phi) \left[h(\zeta) \otimes F + \frac{i\beta_2 l}{2} h(\zeta) \otimes \frac{\partial^2 F}{\partial \zeta^2} + i\gamma l h(\zeta) \otimes |F|^2 F \right]. \quad (6)$$

We focus our analysis to high-finesse cavities. This means that the transmission coefficient θ is assumed to be much smaller than unity $\theta \ll 1$, so that the reflection coefficient is $\rho \approx 1 - \theta^2/2$. We also assume that the linear phase shift acquired by the light is small $\phi \ll 1$ over the length l , so that $\exp(i\phi) \approx (1 + i\phi)$. Under these approximations,

Eq. (6) reads

$$t_r \frac{\partial F}{\partial t} = \theta F_i - F + \left(1 - \frac{\theta^2}{2} - i\phi\right) \left[h(\zeta) \otimes F + \frac{i\beta_2 l}{2} h(\zeta) \otimes \frac{\partial^2 F}{\partial \zeta^2} + i\gamma l h(\zeta) \otimes |F|^2 F \right]. \quad (7)$$

This equation is an integrodifferential equation containing three convolution terms. It is derived from an infinite-dimensional map equations (1) and (2) via averaging over a cavity length and by introducing continuous time and its derivative in the double limit of high-finesse cavities $\theta \ll 1$ and small linear phase shift $\phi \ll 1$.

B. Generalized Lugiato-Lefever equation with spectral filtering

To describe the evolution of the intracavity field, we use the mean-field approach to further simplify the integrodifferential equation Eq. (7) into a partial differential equation. Before applying the mean-field approximation, let us first evaluate the three convolutions that appear in Eq. (7). The causal convolution term $h(\zeta) \otimes F(t, \zeta)$ is

$$h(\zeta) \otimes F(t, \zeta) = \int_0^{+\infty} h(\zeta') F(t, \zeta - \zeta') d\zeta'. \quad (8)$$

Expanding the term $F(t, \zeta - \zeta')$ in a Taylor series, one gets

$$\begin{aligned} h(\zeta) \otimes F(t, \zeta) &= \int_0^{+\infty} h(\zeta') \sum_{n=0}^{\infty} (-1)^n \frac{\zeta'^n}{n!} \frac{\partial^n F}{\partial \zeta^n} d\zeta', \\ &= \sum_{n=0}^{\infty} a_n \frac{\partial^n F}{\partial \zeta^n}, \end{aligned} \quad (9)$$

the coefficients a_n are

$$a_n(\zeta) = (-1)^n \int_0^{+\infty} h(\zeta') \frac{\zeta'^n}{n!} d\zeta'. \quad (10)$$

The above coefficients are well defined for functions $h(\zeta)$ that decay faster than a polynomial. Given this restriction, we get

$$h(\zeta) \otimes F(t, \zeta) = a_0 F + a_1 \frac{\partial F}{\partial \zeta} + a_2 \frac{\partial^2 F}{\partial \zeta^2} + \dots \quad (11)$$

A similar calculation leads to the evaluation of the two other convolutions in the integrodifferential Eq. (7), namely,

$$h(\zeta) \otimes \frac{\partial^2 F}{\partial \zeta^2} = c_0 \frac{\partial^2 F}{\partial \zeta^2} + c_1 \frac{\partial^3 F}{\partial \zeta^3} + \dots, \quad (12)$$

$$h(\zeta) \otimes |F|^2 F = d_0 |F|^2 F + d_1 \frac{\partial |F|^2 F}{\partial \zeta} + \dots \quad (13)$$

Replace the above three convolution terms Eqs. (11) to (13) into the integrodifferential Eq. (7). Also, assume that the nonlinear phase shift must be smaller than unity, i.e., $\gamma l |F|^2 \ll 1$. Finally, assume that the cavity length is much shorter than the characteristic dispersion length of the field. Under these approximations, this equation reduces to the following

generalized Lugiato-Lefever equation (see the Appendix)

$$\begin{aligned} \partial_t E &= E_i - (\kappa + i\delta)E + i|E|^2 E + i\alpha_1 \frac{\partial E}{\partial \zeta} + (\alpha_2 + i\beta) \frac{\partial^2 E}{\partial \zeta^2} \\ &\quad + i\alpha_3 \frac{\partial^3 E}{\partial \zeta^3} + i\alpha_4 \frac{\partial |E|^2 E}{\partial \zeta} + \text{h.o.t.}, \end{aligned} \quad (14)$$

where $\kappa = (1 - a_0 + a_0 \theta^2/2)/t_r$, $\alpha_1 = -\phi a_1/(1 - a_0 + a_0 \theta^2/2)$, and h.o.t. are the higher-order terms in the amplitude E in its fast-time derivatives and nonlinear terms.

This model equation is very general as it does not specify the exact form of the transfer function nor the filter frequency. The presence of the filter impacts the formation of dissipative solitons by four contributions: diffusion, linear, and nonlinear convection, and third-order dispersion with *purely imaginary* coefficients.

To reduce further the complexity of the generalized LLE, we will use a global perturbation scheme based on multiple-scale analysis in the limit of the long cavity ($t_r^{-1} \sim \epsilon \ll 1$, where ϵ is a small parameter) and small linear phase shift $\phi \sim \epsilon^{1/2}$. This method is useful for systems characterized by different timescales [37]. For this purpose, we introduce the following timescales: $\kappa \sim \epsilon$, $\delta \sim \epsilon$, $\alpha_1 \sim \epsilon^{1/2}$, $\beta \sim \alpha_2 \sim \alpha_3 \sim \alpha_4 \sim O(1)$, $|E| \sim \epsilon^{1/2}$, $\partial/\partial t \sim \epsilon$, and $\partial/\partial \zeta \sim \epsilon^{1/2}$. The first five terms on the right side of Eq. (14) are of order $\epsilon^{3/2}$, and the remaining terms are of order ϵ^2 . Then, after renormalizing the coefficients according to the dominant order, the amplitude equation reads

$$\begin{aligned} \partial_t E(t, \tau) &= E_i - (1 + i\delta)E + i|E|^2 E \\ &\quad + i\alpha_1 \frac{\partial E}{\partial \tau} + (\alpha_2 + i\beta) \frac{\partial^2 E}{\partial \tau^2}. \end{aligned} \quad (15)$$

This simple equation ignores high-order terms, such as the third derivative with a purely imaginary coefficient, i.e., $i\alpha_3 \partial^3 E / \partial \zeta^3$. This term cannot be neglected for a filter with a sharp transfer function so that the equation is only valid for smooth ones. Moreover, if the intracavity field strength is low, the nonlinear convective terms with a complex coefficient, i.e., $i\alpha_4 \partial |E|^2 E / \partial \zeta$ can reasonably be ignored. We place our study in this limit.

Taking into account the temporal or spatial filters associated with gain dispersion or diffusion, respectively, in the modeling of the ring cavity filled with Kerr media implies considering not only a diffusive term, $\alpha_2 \partial^2 E$; as in [34,35,38,39], but also the first derivative whose coefficient is purely imaginary; $i\alpha_1 \partial E$. We anticipate that this term will have significant consequences on the dynamics as it produces a new contribution to the phase of light, which can affect both the velocity and shape of the solutions.

III. LINEAR STABILITY ANALYSIS AND MODULATIONAL INSTABILITY

A. Linear stability analysis

The continuous wave solutions (CWs) of Eq. (15) are $E_i^2 = |E_s|^2 [1 + (|E_s|^2 - \delta)^2]$. They are independent of the parameters $\alpha_{1,2}$, and the CWs are, therefore, unaffected by the spectral filtering effect. For $\delta < \sqrt{3}$ ($\delta > \sqrt{3}$), the transmitted intensity as a function of the input intensity E_i^2 is monostable

(bistable). With periodic boundary conditions, we consider small fluctuations $\exp(\lambda t + i\omega\tau)$ around the CW E_s . This formulation leads to a characteristic equation which is quadratic in λ and whose coefficients are functions of ω^2 and the system parameters

$$(\lambda + 1 + \alpha_2\omega^2)^2 + (\delta - 2I_s - i\alpha_1\omega + \beta\omega^2)^2 - I_s^2 = 0, \quad (16)$$

with $I_s = |E_s|^2$. The solutions of the characteristic Eq. (16) reads

$$\lambda_{\pm} = -1 - \alpha_2\omega^2 \pm \sqrt{I_s^2 - (\delta - 2I_s - i\alpha_1\omega + \beta\omega^2)^2}. \quad (17)$$

In the Fourier space, unstable modes are characterized by a finite range of frequencies excluding the origin. This range must exclude all large periods (small frequency) corresponding to quasuniform distributions and very short periods (large frequency). They ensure that temporal fluctuations of arbitrarily small and large frequencies are damped. The well-known temporal modulational instability occurs when the real part of the eigenvalue corresponding to when ω_m changes sign and becomes positive. This dispersion relation determines the critical point associated with modulational instability, provided that $\text{Re}[\lambda(\omega_m)] = 0$ and $\partial_{\omega}\text{Re}[\lambda(\omega_m)] = 0$.

In the case of the spectral filter, where $\alpha_1 \neq 0$ and $\alpha_2 \neq 0$, the threshold and critical frequency expressions at the modulation instability threshold are cumbersome. However, when $\alpha_1 = 0$, in the case of a phase filter, the critical frequency expression is simple and reads as follows:

$$\omega_m^2 = \frac{\beta(2|E_m|^2 - \delta) - \alpha_2}{\alpha_2^2 + \beta^2}, \quad (18)$$

where $|E_m|^2$ is the critical intensity at the onset of the bifurcation and is given by

$$|E_m|^2 = \frac{(\alpha_2\delta - \beta)[2\alpha_2 \pm \sqrt{\alpha_2^2 + \beta^2}]}{3\alpha_2^2 - \beta^2}. \quad (19)$$

In the absence of spectral filtering, i.e., $\alpha_1 = \alpha_2 = 0$, we recover the well-known critical frequency and threshold for the modulational instability: $|E_m|^2 = 1$ and $\omega_m^2 = (2 - \delta)/\beta$ obtained for $\beta = 1$ [18]. Considering a small filter strength ($\alpha_2 \ll 1$), solutions with a minus sign should be excluded since the intensity is positively defined.

Let us first consider the anomalous dispersion regime where the chromatic dispersion coefficient is positive, i.e., $\beta > 0$ and focus on the monostable case where the output is a single-valued function of the injected field amplitude, i.e., $\delta < \sqrt{3}$. Figure 2 shows the input-output characteristics and the marginal stability curves for different values of $\alpha = \alpha_1 = \alpha_2$. The threshold associated with modulational instability is shifted towards a higher injected field strength, indicating that the spectral filter tends to stabilize the CWs as shown in Fig. 2(a). The period of temporal structures emerging from the modulatory instability is affected by the α_2 parameter, as shown in Fig. 2. In the monostable regime, i.e., $\delta < \sqrt{3}$, we see that the threshold associated with the modulational instability is increased with the spectral filtering coefficients. In the bistable regime we shall analyze the stability separately from the three CW solutions, forming a bistable response curve when $\sqrt{3} < \delta < \delta_l$, with $\delta_l = [-\alpha_2 + 2(\alpha_2^2 + \beta^2)^{1/2}]/\beta$ in

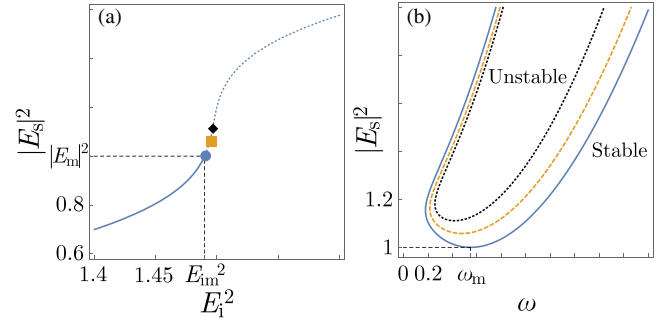


FIG. 2. (a) CWs of Eq. (15) in the monostable case for anomalous dispersion where the threshold of the modulational instability is shown with markers for different values of $\alpha_1 = \alpha_2 = \alpha$. The blue dot corresponds to $\alpha = 0$, the orange square to $\alpha = 0.2$, and the black diamond to $\alpha = 0.4$. (b) Marginal stability curve for the frequency as a function of the CW intensity obtained from the real part of Eq. (17). The blue full line corresponds to $\alpha = 0$, the orange dashed to $\alpha = 0.2$, and the black dotted line to $\alpha = 0.4$. Other parameters are $\delta = 1.7$, $\beta = 1$.

the case $\alpha_1 = 0$, a small portion of the lower CW solution is affected by the modulational instability (MI), namely, in the range

$$|E_m|^2 < |E_s|^2 < |E_l|^2. \quad (20)$$

$|E_l|^2 = [2\delta - (\delta^2 - 3)^{1/2}]/3$ is the lower limit or turning point associated with the bistable response curve. The intermediate CW solution is always unstable even in the absence of chromatic dispersion. The upper CW solution is unstable for all input injection values. Therefore, when $\sqrt{3} < \delta < \delta_l$, the bistable response curve is unstable when $|E_s|^2 > |E_m|^2$. The expression for δ_l is obtained by replacing $|E_m|^2$ from Eq. (19) in Eq. (18) and solving $\omega_m^2 = 0$ for δ . In the absence of spectral filtering, i.e., when $\alpha_1 = \alpha_2 = \alpha = 0$, we recover the frequency range $\sqrt{3} < \delta < 2$ for which a small portion of the lower CW solution is linearly unstable, namely, in the range $1 < |E_s|^2 < |E_l|^2$. For $\delta = \delta_l$, the dissipative MI threshold coincides with the lower limit point associated with bistability, i.e., $|E_m|^2 = |E_l|^2$.

For $\delta \geq \delta_l$ the upper (lower) CW solution remains unstable (stable) for all values of the injected field. This situation is shown in Fig. 3, where the left panel depicts the stabilization of the lower CW as α_2 increases.

In the normal dispersion regime where the chromatic dispersion coefficient is negative, i.e., $\beta < 0$, the modulational instability does not affect the monostable regime. However, in the bistable case, a small portion of the lower CWs becomes modulationally unstable. By increasing the strength of the spectral filtering, both states forming the hysteresis loop of the bistable output-input characteristic become modulationally stable. This result is shown in Fig. 4(a) where the threshold of the modulational instability is pushed towards the upper limit point as α increases. The corresponding behavior of the marginal stability curve is presented in Fig. 4(b). The blue curve obtained in the absence of filtering shows a single instability threshold with a critical frequency given by $\omega_m = \sqrt{(2 - \delta)/|\beta|}$. Nonzero spectral filtering induces a deformation of the marginal stability curve, as seen on the orange

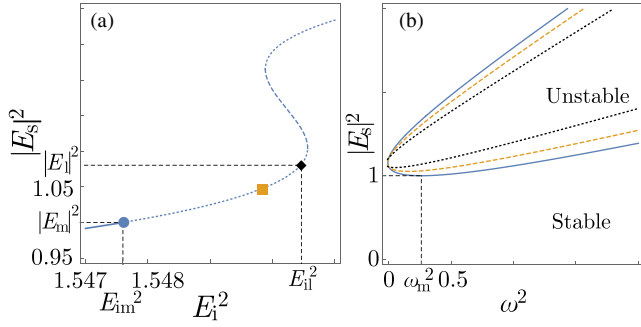


FIG. 3. (a) CWs of Eq. (15) in the bistable case for anormal dispersion where the threshold of the modulational instability is shown with markers for different values of $\alpha_1 = 0$, $\alpha_2 = \alpha$. The blue dot corresponds to $\alpha = 0$, the orange square to $\alpha = 0.2$, and the black diamond to $\alpha = 0.4$. (b) Marginal stability curve for the frequency as a function of the CW intensity obtained from the real part of Eq. (17). The blue full line corresponds to $\alpha = 0$, the orange dashed line to $\alpha = 0.2$, and the black dotted line to $\alpha = 0.4$. Other parameters are $\delta = 1.74$, $\beta = 1$.

curve. As the filtering intensity increases further, the modulational instability threshold approaches the lower limit point of the bistable cycle, leading to stabilisation of the lower CW solutions (see Fig. 4). In what follows, we will concentrate our analysis on the anomalous dispersion regime, i.e., $\beta < 0$.

B. Temporal periodic structures

The linear regime discussed in the previous section allows to determine the thresholds as well as the frequencies at the modulational instability. We now explore numerically the nonlinear dynamics above the modulational instability threshold. We fix all the parameters as $\delta = 1.7$, $\beta = 1$, $\alpha_1 = 0.1$, $\alpha_2 = 0.1$ and we vary the injected field amplitude as the control parameter. As the input field increases, the CW solution becomes modulationally unstable, and the output field spontaneously develops a periodic structure with a

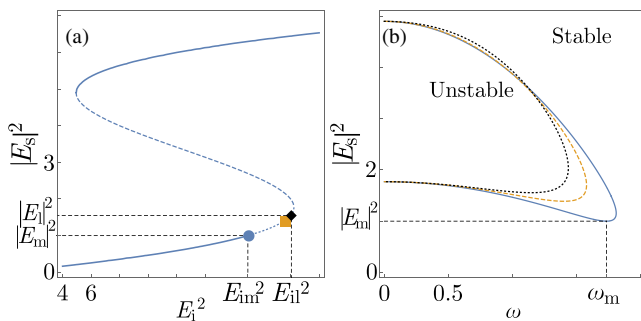


FIG. 4. (a) CWs of Eq. (15) in the bistable case for normal dispersion where the threshold of the modulational instability is shown with markers for different values of $\alpha_1 = \alpha_2 = \alpha$. The blue dot corresponds to $\alpha = 0$, the orange square to $\alpha = 0.2$, and the black diamond to $\alpha = 0.4$. (b) Marginal stability curve for the frequency as a function of the CW intensity obtained from real part of Eq. (17). The blue full line corresponds to $\alpha = 0$, the orange dashed line to $\alpha = 0.2$, and the black dotted line to $\alpha = 0.4$. Other parameters are $\delta = 5$, $\beta = -1$.

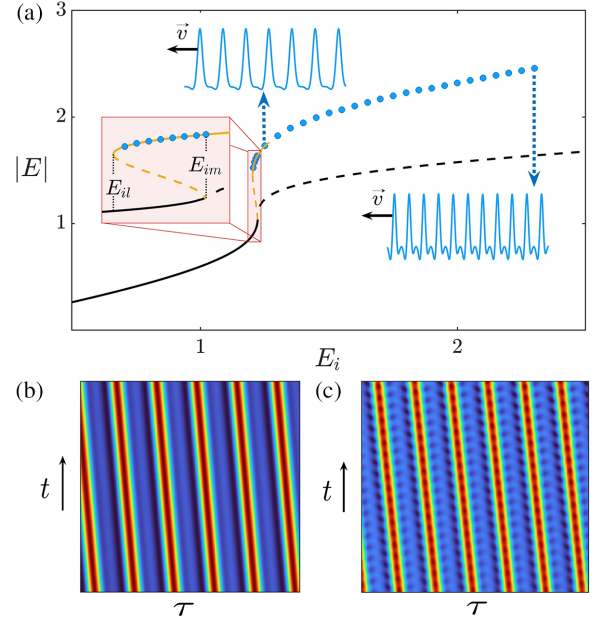


FIG. 5. Bifurcation diagram obtained in the monostable case. (a) The amplitude of the intracavity field as a function of the amplitude of the injected field. The black curve represents the CW solutions. The solid (dashed) line indicates stable (unstable) with respect to modulational instability. The blue dots indicate the maximum amplitude of moving periodic structures. The modulational instability appears to be subcritical. A hysteresis loop exists in the range $E_{il} < E_i < E_{im}$ between stable CW solutions and moving periodic structures. A continuation algorithm generates the unstable and stable mustard curves resulting from the modulation instability, while the blue dots correspond to direct numerical simulations of Eq. (15). (b,c) The $\tau - t$ maps obtained for $E_i = 2.3$ and $E_i = 2.39$, respectively, associated with regular moving periodic structures and breathing structures. Other parameters are $\delta = 1.7$, $\beta = 1$, $\alpha_1 = 0.1$, and $\alpha_2 = 0.1$.

well-defined frequency or period. Using the implicit Euler algorithm scheme, they are obtained from numerical simulations of the mean-field model Eq. (15). Numerically, this is done using periodic boundary conditions compatible with the resonator geometry in Fig. 1. The grid size is 500 with a temporal step integration size of 0.1. We consider the monostable regime where the CW solution is a single-valued function of the injection beam. This solution is shown by the black line in Fig. 5(a) and is stable until the threshold denoted by E_{im} . Above this threshold, the CW solutions become unstable and develop spontaneously moving periodic structures. An example of this solution is plotted in the $\tau - t$ map in Fig. 5(b). An example of such temporal profile of the intracavity field amplitude moving with a constant speed \bar{v} is shown above the curves. The amplitude of regular moving periodic solutions as a function of the input amplitude is indicated by blue dots in the bifurcation diagram of Fig. 5(a). The motion is directly attributed to the presence of spectral filtering, which generates through mean-field modeling a term $i\alpha_1 \partial_\tau E$ in the generalized LLE model Eq. (15). The presence of this term breaks the reflection symmetry $\tau \rightarrow -\tau$ leading to traveling solutions.

When the input field intensity is decreased, the periodic solution remains stable in the range of $E_{il} < E_i < E_{im}$ as

shown in the zoom of Fig. 5(a). Indeed, the branch of moving periodic solution emerges subcritically from the modulational instability and is connected to the CW solution by unstable solutions represented by a dashed line as shown in the zoom of Fig. 5(a). These unstable and stable branches of solutions are obtained by the pseudo-arclength continuation method, which allows the plotting of both stable and unstable periodic traveling solutions (mustard curves). As the input field is further increased beyond the threshold of modulational instability, the output of the resonator evolves from regular to breathing self-pulsating structures. These solutions are moving with speed \bar{v} . The $\tau - t$ map in Fig. 5(c) shows examples of a $t - \tau$ map of the breathing solutions. An example of temporal profile is shown under the curves of Fig. 5(a).

IV. DISSIPATIVE SOLITON COMBS WITH FILTERING

A. Moving and breathing dissipative soliton

Kerr resonators support temporal dissipative solitons in the anomalous dispersion regime where the modulational instability appears subcritically [20]. Their formation does not require a bistability between CW solutions. They can be generated in the monostable regime in the range $\delta < \sqrt{3}$. We consider the input field amplitude domain $E_{il} < E_i < E_{im}$, which gives rise to a hysteresis loop involving the CW solution and the traveling periodic solutions [see the zoom of Fig. 5(a)]. As we shall see, different types of localized solutions exist as stable solutions associated with this domain. Numerical simulations of the generalized LLE model Eq. (15) show evidence of dissipative solitons. The results are summarized in Fig. (6). When $\alpha = 0$, LSs are stationary and symmetric solutions [see Fig. 6(b)]. Their range of existence as stable solutions, indicated by full squares, is rather large, as shown in Fig. 6(a). From this chart, we see that as the spectral filter parameters increase, the dissipative solitons stability range is reduced. In addition, we plot together with the points corresponding to the localized states for $\alpha_1 = 0.1$, the branch of the moving periodic solutions that connects to the CW solution by an unstable solution represented by a dashed line as shown in Fig. 6(a). The branches of the periodic solutions in motion for $\alpha = 0$ and $\alpha = 0.05$ are not shown in Fig. 6(a) for readability. The unstable and stable branches of the periodic solutions are obtained using the pseudoarclength continuation method. The stable branch of the moving periodic solution coincides with the localized branch of the solutions represented by the black dots. However, as we shall see, unlike the periodic solutions, the localized solutions branch is not connected to the CW solution.

In addition, when $\alpha_1 \neq 0$, the localized peaks become asymmetric and begin to exhibit regular motion, as shown in the $\tau - t$ map in Fig. 6(c). The profile of a single peak dissipative soliton is shown in Fig. 6(d). The dissipative soliton has an exponentially decaying tail. The zoomed inset depicts how the asymmetry of the tail becomes more pronounced as the parameter α_1 is increased. The motion is then due to the presence of temporal spectral filtering inside the cavity. The speed of single peak dissipative solitons as a function of the parameter α_1 is plotted in Fig. 6(e). The speed increases with the parameter α_1 and decreases with α_2 . The Fourier transform

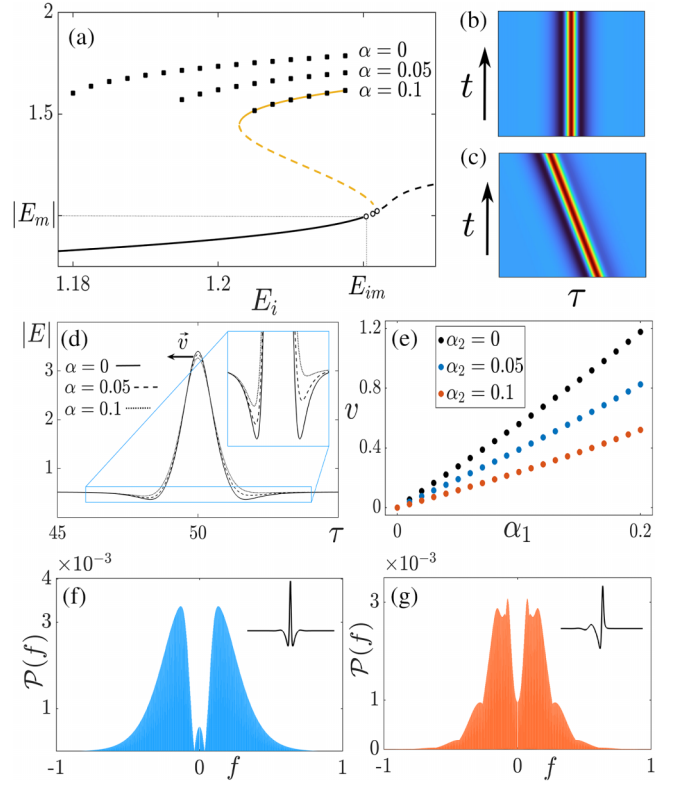


FIG. 6. Moving dissipative solitons obtained in the monostable case. (a) Maximum amplitude of the intracavity field associated with dissipative solitons as a function of the amplitude of the injected field. The black curve represents the CW solutions. As the input field increases, the CW solutions become unstable with respect to modulational instability. The black open circles on this curve represent the threshold associated with modulational instability for $\alpha = 0$, $\alpha = 0.05$, and $\alpha = 0.1$. The solid (dashed) line indicates stable (unstable) with respect to modulational instability. The three curves formed by black squares obtained for $\alpha = 0$, $\alpha = 0.05$, and $\alpha = 0.1$ show the maximum amplitude of moving dissipative structures. (b) $\tau - t$ maps obtained for $E_i = 1.21$, $\alpha_1 = 0$, and $\alpha_2 = 0.1$ associated with stationary dissipative soliton. (c) $\tau - t$ maps obtained for $E_i = 1.21$, $\alpha_1 = 0.2$, and $\alpha_2 = 0.1$ associated with moving dissipative soliton. (d) Zoom-in on the dissipative solitons profile shows the deformation of the soliton tails for different values of the filter parameters. (e) Speed of dissipative solitons for a fixed amplitude of the injected field amplitude as a function of the parameter α_1 . (f,g) Combs associated with the stationary and moving dissipative solitons shown in (b) and (c), respectively. Other parameters are $\delta = 1.7$ and $\beta = 1$.

of the train of localized structures corresponding to Fig. 6(b) and exiting the resonator is plotted in Fig. 6(f). Similarly, the Fourier transform of the moving localized structures shown in Fig. 6(c) is plotted in Fig. 6(g). When the amplitude of the input field is increased in the monostable regime, localized breathing solutions are unstable because the background, the CW solution, becomes modulationally unstable.

We now consider the bistable regime $\delta > \sqrt{3}$. The linear stability analysis shows that the range over which lower CW solutions are stable increases when considering spectral filtering. We fix the detuning parameter to $\delta = 5$, and we vary the input field amplitude. In the absence of spectral filtering

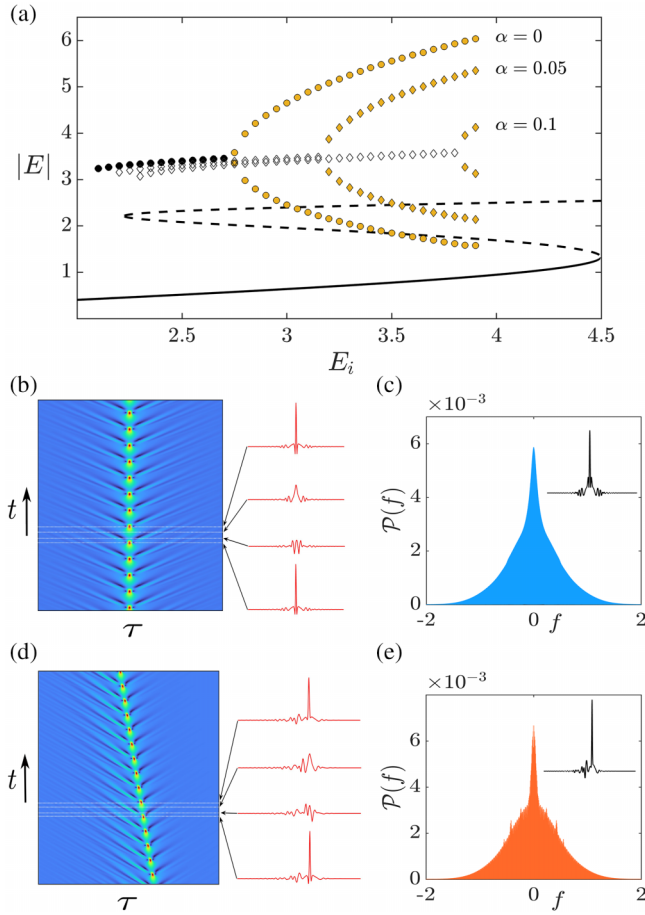


FIG. 7. Moving and breathing dissipative solitons obtained in the bistable case. (a) Maximum amplitude of the intracavity field associated with dissipative solitons as a function of the amplitude of the injected field for different values of $\alpha_1 = \alpha_2 = \alpha$. The black curve represents the CW solutions. The lower branch shown is always stable for $\delta = 5$, and the upper CW solution denoted by the dashed line is always unstable. The three curves formed by circles and diamonds are obtained for $\alpha = 0$, $\alpha = 0.05$, and $\alpha = 0.1$ and show the maximum amplitude of dissipative structures. As the injected field amplitude is increased, the stationary (full circles) and moving (empty diamonds) dissipative soliton branches exhibit a pitchfork bifurcation. Above this bifurcation, the DSs begin to breathe. The two branches emerging from each of these bifurcations represent the maximum and minimum amplitudes associated with the breathing dissipative solitons (yellow circles and diamonds). (b) $\tau - t$ maps obtained for $E_i = 3.9$, $\alpha = 0$ associated with breathing dissipative soliton. (d) $\tau - t$ maps obtained for $E_i = 3.9$, $\alpha_1 = 0.2$, and $\alpha_2 = 0.03$ associated with moving, breathing dissipative soliton. (c,e) Combs associated with stationary and moving dissipative solitons are shown in (b) and (d), respectively. Parameters are $\delta = 5$ and $\beta = 1$.

$\alpha = 0$, numerical simulations of the generalized LLE Eq. (15) show stationary dissipative solitons [the branch of full black circles in Fig. 7(a)]. These regular dissipative solitons are stationary solutions similar to those shown in the monostable case [see Fig. 6(b)]. When the input field is increased, DSs start to exhibit breathing behavior indicated by the yellow branches of maxima and minima in Fig. 7(a). An example is shown in Fig. 7(b). The corresponding comb is plotted in

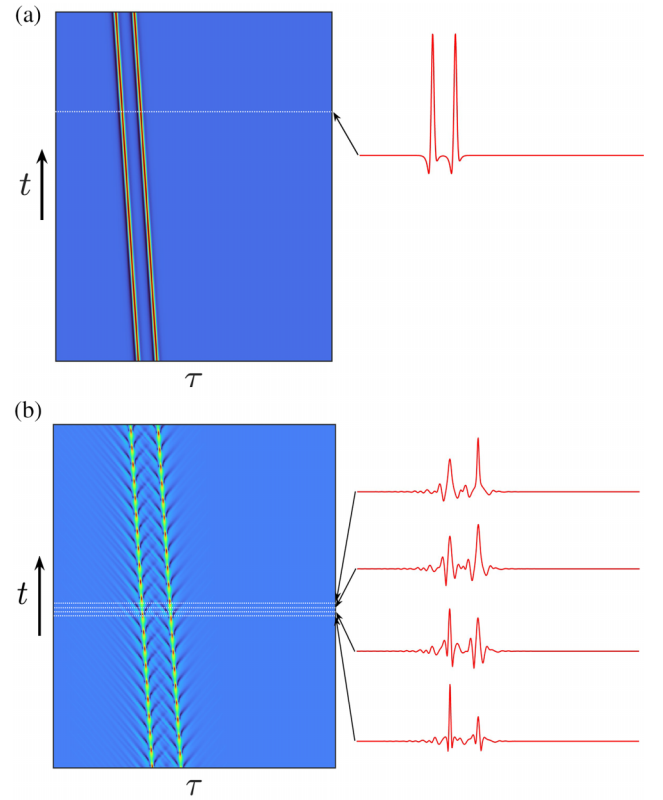


FIG. 8. Bounded dissipative solitons in the presence of spectral filtering. (a) Bounded moving dissipative solitons and (b) bounded moving and breathing dissipative solitons obtained for the same parameters of Figs. 7(b) and 7(d), respectively.

Fig. 7(c). When taking into account spectral filtering, $\alpha \neq 0$, the breathing solitons start to move with a constant speed as shown in Fig. 7(d), and the corresponding comb is plotted in Fig. 7(e).

Kerr micro and macroresonators can host bounded moving solutions. Figure 8(a) shows an example of two bounded moving dissipative solitons. Breathing and moving bounded dissipative solitons are also stable solutions of the generalized LLE model Eq. (15). This solution is shown in Fig. 8(b). Dissipative solitons interact via their exponentially decaying tails and form bounded states. Their weak interaction can be strongly affected by various perturbations, such as periodic modulation [40,41] and high-order dispersions [29,42]. These perturbations lead to the appearance of the so-called soliton Cherenkov radiation at the soliton tails [43,44]. A deeper investigation of interaction in the presence of filtering will be the subject of future publication.

B. Homoclinic snaking bifurcation and isolas of dissipative solitons

Kerr resonators exhibit a high degree of multistability over a finite range of injected field amplitude values, often referred to as the pinning region [45]. More precisely, the generalized LLE model Eq. (15) supports not only two peaks solutions bounded together, but two sets of odd and even localized peaks. Let us first assume that $\alpha_1 = 0$, for which Eq. (15)

admits two snaking curves; one describes dissipative solitons with an odd number $2n + 1$ of peaks, and the other corresponds to an even number $2n$ of peaks, with n a positive integer. They are motionless solutions because the generalized LLE model Eq. (15) conserves the reflection symmetry $\tau \rightarrow -\tau$. Dissipative solitons exhibit a well-known homoclinic snaking type of bifurcation within the subcritical modulational instability range. In the time domain, their bifurcation diagram consists of two snaking curves that are connected and emerge from the modulational instability threshold [46,47]. Since the maximum amplitudes of DSs with different numbers of peaks are close to each other, it is more convenient to plot the L2-norm

$$\mathcal{N} = \int d\tau |E - E_s|^2 \quad (21)$$

as a function of injected field amplitude. The homoclinic snaking bifurcation is shown in Fig. 9. The two snaking curves associated with odd and even numbers of localized peaks are intertwined. They correspond to the back-and-forth oscillations across the pinning region. This feature has been abundantly addressed for the Lugiato-Lefever model without spatial filtering. However, when $\alpha_1 \neq 0$, the classic homoclinic snaking type of bifurcation is broken, and branches of localized peaks form isolas, closed curves disconnected from the CW solutions. This means that the unstable branch associated with the dissipative soliton is not connected to the modulational instability threshold. This property is inherent to all irreversible systems in which the reflection symmetry is broken, i.e., $\tau \not\rightarrow -\tau$. The summary of this analysis is shown in Fig. 10. The bifurcation diagram for moving periodic solutions (green curve) and a dissipative soliton with a single peak (blue curve) are shown in Fig. 10(a). A zoom of the isola branch of the single DS is depicted in Fig. 10(b). The stable (unstable) moving dissipative solitons is shown in full (dashed) line. Profiles corresponding to the points A to D along this isola are indicated in the bottom left corner of the figure, with the profile A being the only stable solution. The associated speeds are shown in Fig. 10(b), where it can be noted that increasing the injection results in an increase of the velocity of the stable DSs.

LLE Eq. (15) without the effect of spectral filtering is known to present a homoclinic snaking bifurcation diagram. However, taking spectral filtering into account, the first $i\alpha_1 \partial_\tau E$ derivative term in Eq. (15) is unavoidable, leading the homoclinic snaking bifurcation to be broken and the dissipative solitons to become asymmetric and exhibit motion. This is a behavior well known in the field of dynamical systems theory [48]. In optics, isolas are also generated by the odd order of dispersion [49] or by Raman scattering [50], which both break the parity symmetry.

V. CONCLUSION

We studied the formation of temporal dissipative solitons and the corresponding combs generation in driven resonators under the combined influence of the Kerr effect, dispersion, dissipation, and spectral filtering. We generalized the well-known mean-field Lugiato-Lefever model. The equation was derived from the infinite-dimensional Ikeda map with a gen-

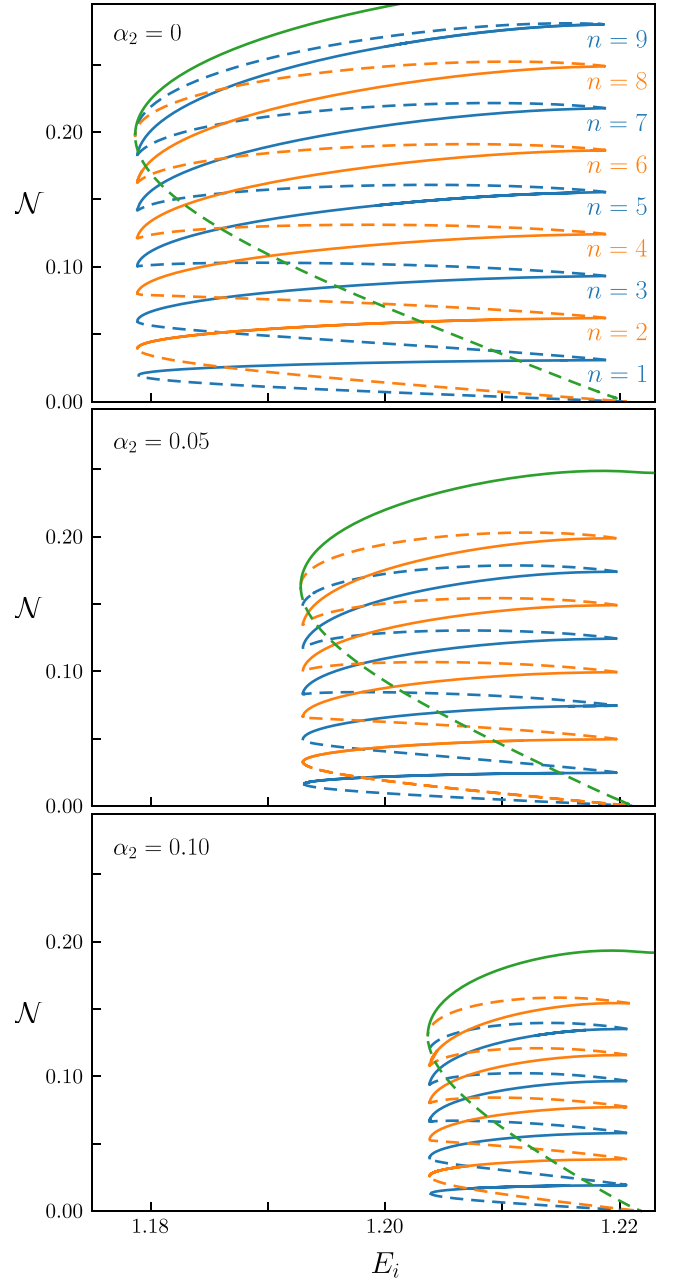


FIG. 9. Bifurcation diagram showing the L2-norm $\mathcal{N} = \int d\tau |E - E_s|^2$ as a function of the injection amplitude E_i . Green lines indicate periodic solutions, while (orange) blue lines indicate (even) odd numbers of peaks in localized states. Full (dashed) lines correspond to stable (unstable) states, respectively. Parameters are $\delta = 1.7$, $\beta = 1$, $\alpha_1 = 0$.

eral impulse response function. We used a global perturbation scheme based on multiscale analysis to further simplify this model by removing high-order terms such as third-order dispersion i.e., $i\alpha_3 \partial^3 E / \partial \zeta^3$ and nonlinear convective terms, i.e., $i\alpha_4 \partial |E|^2 E / \partial \zeta$. The simplified equation was only valid in cases of low intracavity field strength and smooth transfer functions.

It was shown that, in addition to the second-order derivative with a fast response time associated with the gain dispersion, an additional first-order derivative with a purely imaginary

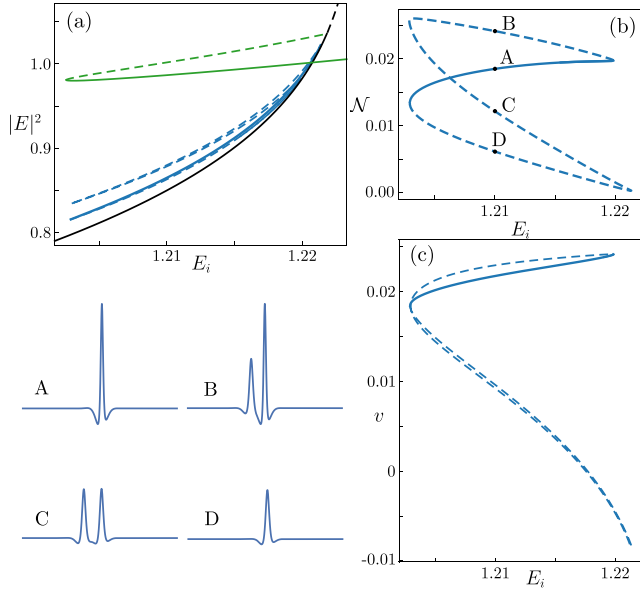


FIG. 10. Dissipative solitons isolas. (a) Bifurcation diagram showing the intensity of the intracavity field as a function of the injected field amplitude E_i . Black lines indicate the CWs, green lines indicate the intensity of moving periodic solutions, and blue lines indicate the one-peak dissipative soliton. (b) L2-norm of the dissipative soliton branch as a function of the injected field amplitude. (c) Velocity of moving dissipative solitons isolas as a function of the injected field amplitude E_i . Full (dashed) lines correspond to stable (unstable) states, respectively. Parameters are $\delta = 1.7$, $\beta = 1$, and $\alpha_1 = \alpha_2 = \alpha = 0.1$.

coefficient $i\alpha_1 \partial E / \partial \tau$ is necessary for the modeling. This term has a significant impact on the dynamics and results in the following consequences.

(i) The CW solutions are stabilized as the modulational instability threshold is shifted towards higher intensity. Numerical simulations generate moving and breathing patterns. A branch of moving solutions connecting these periodic solutions to the modulational instability has been constructed using a continuation algorithm.

(ii) In the monostable regime, where the CW solutions are single-valued functions of the injection field, the spectral filtering not only breaks the reflection symmetry that causes dissipative solitons to move, but also reduces the stability domain associated with moving dissipative solitons (cf. Fig. 6).

(iii) In the bistable regime, the stability domain of moving dissipative solitons is enlarged by the spectral filtering, as the threshold above which transition to breathing dissipative solitons occurs is shifted towards higher injected field intensity (cf. Fig. 7). Numerical simulations revealed the existence

of moving bounded dissipative solitons, including moving-breathing bounded dissipative solitons.

(iv) The first derivative term breaks the homoclinic snaking type of bifurcation and promotes rather the formation of isolas branches of dissipative solitons.

Further work is needed to complete the picture and characterize the whole bifurcation structure showing isolas stacking associated with multippeak dissipative solitons, using numerical continuation methods. The same behavior will be investigated in two-dimensional diffractive Kerr resonators under spatial filtering.

ACKNOWLEDGMENTS

We thank A. G. Vladimirov for enlightening discussions. M.B.G. and M.G.C. acknowledge the financial support of ANID-Millennium Science Initiative Program-ICN17_012 (MIRO) and FONDECYT Project No. 1210353. M.T. is a Research Director at Fonds de la Recherche Scientifique FNRS.

APPENDIX: ADIMENSIONAL GENERALIZED LLE WITH FILTERING

To derive the adimensional form Eq. (14) we start from Eq. (7) and insert expressions Eqs. (11) to (13) for the three convolution terms, we get

$$\begin{aligned} t_r \frac{\partial F}{\partial t} = & \theta F_i - F + \left(1 - \frac{\theta^2}{2} - i\phi\right) \left(a_0 F + a_1 \frac{\partial F}{\partial \zeta} + a_2 \frac{\partial^2 F}{\partial \zeta^2}\right) \\ & + \frac{i\beta_2 l}{2} \left(c_0 \frac{\partial^2 F}{\partial \zeta^2} + c_1 \frac{\partial^3 F}{\partial \zeta^3}\right) \\ & + i\gamma l \left(d_0 |F|^2 F + d_1 \frac{\partial |F|^2 F}{\partial \zeta}\right). \end{aligned} \quad (\text{A1})$$

Using the following changes of variables and scalings:

$$\begin{aligned} E = F \sqrt{\gamma l d_0 \sigma}, \quad E_i = \theta F_i \sigma \sqrt{\gamma l d_0 \sigma}, \quad t = \frac{1}{t_r \sigma} t, \quad \delta = a_0 \phi \sigma, \\ v = (1 - \theta^2/2) a_1 \sigma, \quad \alpha_1 = -\phi a_1 \sigma, \quad \alpha_2 = a_2 \sigma, \quad \beta = \frac{\beta_2 l}{2} \sigma c_0, \\ \alpha_3 = \frac{\beta_2 l}{2} \sigma c_1, \quad \alpha_4 = \frac{d_1}{d_0}, \quad \text{with } \sigma = \kappa / \left(1 - a_0 + a_0 \frac{\theta^2}{2}\right) \end{aligned}$$

leads to the dimensionless form Eq. (14)

$$\begin{aligned} \frac{\partial E}{\partial t} = & E_i - (\kappa + i\delta) E + i|E|^2 E + (v + i\alpha_1) \frac{\partial E}{\partial \zeta} \\ & + (\alpha_2 + i\beta) \frac{\partial^2 E}{\partial \zeta^2} + i\alpha_3 \frac{\partial^3 E}{\partial \zeta^3} + i\alpha_4 \frac{\partial |E|^2 E}{\partial \zeta}. \end{aligned} \quad (\text{A2})$$

According to Eq. (10), $a_i = c_i = d_i$, with $i = 0, 1, 2$, and by considering the comoving reference system, $\tau = \zeta + vt$, the model Eq. (A2) becomes Eq. (15).

[1] A. Pasquazi *et al.*, *Phys. Rep.* **729**, 1 (2018).

[2] T. Fortier and E. Baumann, *Commun. Phys.* **2**, 153 (2019).

[3] N. Picqué and T. H. Hänsch, *Nat. Photonics* **13**, 146 (2019).

[4] C. Bao, Y. Chembo, M. Erkintalo, T. Herr, A. Matsko, Y. Okawachi, and M. Tlidi, *IEEE Journal of Selected Topics in Quantum Electronics* **30**, 0001801 (2024).

[5] T. H. Hänsch, *Rev. Mod. Phys.* **78**, 1297 (2006).

[6] T. Herr, V. Brasch, J. D. Jost, C. Y. Wang, N. M. Kondratiev, M. L. Gorodetsky, and T. J. Kippenberg, *Nat. Photonics* **8**, 145 (2014).

[7] T. J. Kippenberg, A. L. Gaeta, M. Lipson, and M. L. Gorodetsky, *Science* **361**, eaan8083 (2018).

- [8] P. Del’Haye, A. Schliesser, O. Arcizet, T. Wilken, R. Holzwarth, and T. G. Kippenberg, *Nature (London)* **450**, 1214 (2007).
- [9] S. B. Papp, K. Beha, P. Del’Haye, F. Quinlan, H. Lee, K. J. Vahala, and S. A. Diddams, *Optica* **1**, 10 (2014).
- [10] M. G. Suh and K. J. Vahala, *Science* **359**, 884 (2018).
- [11] D. T. Spencer *et al.*, *Nature (London)* **557**, 81 (2018).
- [12] B. Min, L. Yang, and K. Vahala, *Appl. Phys. Lett.* **87**, 181109 (2005).
- [13] W. Liang, V. S. Ilchenko, A. A. Savchenkov, A. B. Matsko, D. Seidel, and L. Maleki, *Phys. Rev. Lett.* **105**, 143903 (2010).
- [14] M. Karpov, H. Guo, A. Kordts, V. Brasch, M. H. P. Pfeiffer, M. Zervas, M. Geiselmann, and T. J. Kippenberg, *Phys. Rev. Lett.* **116**, 103902 (2016).
- [15] X. Liu, C. Sun, B. Xiong, L. Wang, J. Wang, Y. Han, Z. Hao, H. Li, Y. Luo, J. Yan, and H. X. Tang, *ACS Photonics* **5**, 1943 (2018).
- [16] A. Chen-Jinnai, T. Kato, S. Fujii, T. Nagano, T. Kobatake, and T. Tanabe, *Opt. Express* **24**, 26322 (2016).
- [17] S. Zhu, L. Shi, L. Ren, Y. Zhao, B. Jiang, B. Xiao, and X. Zhang, *Nanophotonics* **8**, 2321 (2019).
- [18] L. A. Lugiato and R. Lefever, *Phys. Rev. Lett.* **58**, 2209 (1987).
- [19] Y. K. Chembo, D. Gomila, M. Tlidi, and C. R. Menyuk, *Eur. Phys. J. D* **71**, 299 (2017).
- [20] A. J. Scroggie, W. J. Firth, G. S. McDonald, M. Tlidi, R. Lefever, and L. A. Lugiato, *Chaos Solitons Fractals* **4**, 1323 (1994).
- [21] M. Tlidi, P. Mandel, and R. Lefever, *Phys. Rev. Lett.* **73**, 640 (1994).
- [22] A. B. Matsko, A. A. Savchenkov, W. Liang, V. Ilchenko, D. Seidel, and L. Maleki, *Opt. Lett.* **36**, 2845 (2011).
- [23] S. Coen, H. G. Randle, T. Sylvestre, and M. Erkintalo, *Opt. Lett.* **38**, 37 (2013).
- [24] L. A. Lugiato, F. Prati, M. Gorodetsky, and T. J. Kippenberg, *Philos. Trans. R. Soc. A* **376**, 20180113 (2018).
- [25] M. Tlidi, M. Clerc, and K. Panajotov, *Philos. Trans. R. Soc. A* **376**, 20180114 (2018).
- [26] M. G. Clerc, S. Coulibaly, and M. Tlidi, *Phys. Rev. Res.* **2**, 013024 (2020).
- [27] M. G. Clerc, S. Coulibaly, P. Parra-Rivas, and M. Tlidi, *Chaos* **30**, 083111 (2020).
- [28] P. Parra-Rivas, S. Coulibaly, M. G. Clerc, and M. Tlidi, *Phys. Rev. A* **103**, 013507 (2021).
- [29] M. Tlidi, L. Bahloul, L. Cherbi, A. Hariz, and S. Coulibaly, *Phys. Rev. A* **88**, 035802 (2013).
- [30] M. Tlidi, A. G. Vladimirov, D. Pieroux, and D. Turaev, *Phys. Rev. Lett.* **103**, 103904 (2009).
- [31] F. Bessin, A. M. Perego, K. Staliunas, S. K. Turitsyn, A. Kudlinski, M. Conforti, and A. Mussot, *Nat. Commun.* **10**, 4489 (2019).
- [32] S. Negrini, J. B. Ceppe, M. Conforti, A. M. Perego, A. Kudlinski, and A. Mussot, *Opt. Express* **31**, 37011 (2023).
- [33] A. M. Perego, A. Mussot, and M. Conforti, *Phys. Rev. A* **103**, 013522 (2021).
- [34] X. Dong, C. Spiess, V. G. Bucklew, and W. H. Renninger, *Phys. Rev. Res.* **3**, 033252 (2021).
- [35] A. Pimenov and A. G. Vladimirov, *Optics* **3**, 364 (2022).
- [36] A. G. Vladimirov and D. A. Dolinina, *Phys. Rev. E* **109**, 024206 (2024).
- [37] C. M. Bender and S. A. Orzag, *Advanced Mathematical Methods for Scientists and Engineers* (Springer, New York, 1999).
- [38] D. Turaev, A. G. Vladimirov, and S. Zelik, *Phys. Rev. Lett.* **108**, 263906 (2012).
- [39] S. W. Huang, H. Zhou, J. Yang, J. F. McMillan, A. Matsko, M. Yu, D. L. Kwong, L. Maleki, and C. W. Wong, *Phys. Rev. Lett.* **114**, 053901 (2015).
- [40] J. M. Soto-Crespo, N. N. Akhmediev, P. Grelu, and F. Belhache, *Opt. Lett.* **28**, 1757 (2003).
- [41] M. Olivier, V. Roy, and M. Piché, *Opt. Lett.* **31**, 580 (2006).
- [42] A. G. Vladimirov, M. Tlidi, and M. Taki, *Phys. Rev. A* **103**, 063505 (2021).
- [43] N. N. Akhmediev and M. Karlsson, *Phys. Rev. A* **51**, 2602 (1995).
- [44] A. G. Vladimirov, S. V. Gurevich, and M. Tlidi, *Phys. Rev. A* **97**, 013816 (2018).
- [45] Y. Pomeau, *Physica D* **23**, 3 (1986).
- [46] M. Tlidi and L. Gelens, *Opt. Lett.* **35**, 306 (2010).
- [47] P. Parra-Rivas, D. Gomila, M. A. Matias, S. Coen, and L. Gelens, *Phys. Rev. A* **89**, 043813 (2014).
- [48] M. Beck, J. Knobloch, D. J. B. Lloyd, B. Sandstede, and T. Wagenknecht, *SIAM J. Math. Anal.* **41**, 936 (2009).
- [49] P. Parra-Rivas, D. Gomila, F. Leo, S. Coen, and L. Gelens, *Opt. Lett.* **39**, 2971 (2014).
- [50] M. Tlidi, M. Bataille-Gonzalez, M. G. Clerc, L. Bahloul, S. Coulibaly, B. Kostet, C. Casillo-Pinto, and K. Panajotov, *Chaos Solitons Fractals* **174**, 113808 (2023).